Applied Catalysis B: Environmental 327 (2023) 122436

Contents lists available at ScienceDirect

Applied Catalysis B: Environmental

journal homepage: www.elsevier.com/locate/apcatb

Enhanced low temperature performance of bimetallic $Pd/Pt/SiO_2$(core) @Zr(shell) diesel oxidation catalysts☆

Chih-Han Liu [a], Stephen Porter [b], Junjie Chen [a], Hien Pham [b], Eric J. Peterson [c], Prateek Khatri [a], Todd J. Toops [d], Abhaya Datye [b], Eleni A. Kyriakidou [a,*]

[a] Department of Chemical and Biological Engineering, University at Buffalo, The State University of New York, Buffalo, NY 14260, USA
[b] Department of Chemical and Biological Engineering and Center for Micro-Engineered Materials, University of New Mexico, Albuquerque, NM, 87131, USA
[c] Department of Earth and Planetary Sciences, University of New Mexico, Albuquerque, NM 87131, USA
[d] Energy and Transportation Sciences Division, Oak Ridge National Laboratory, Oak Ridge, TN 37831, USA

ARTICLE INFO

Keywords:
Core-shell support
Diesel oxidation catalyst
Hydrothermal stability
Pd/Pt alloy

ABSTRACT

In this study, the diesel oxidation performance of degreened (DG) and hydrothermally aged monometallic and bimetallic $Pd/Pt/SiO_2$(core)@Zr(shell) catalysts with varying Pd/Pt molar ratios from 3/1–1/3 was evaluated. Pd/Pt(3/1)/SiO_2 @Zr (DG) achieved 50% and 90% conversion of CO at 166 °C (T_{50}), 169 °C (T_{90}) and total hydrocarbons (THCs) at 198 °C (T_{50}), 244 °C (T_{90}). Decreasing the Pd/Pt molar ratio led to a decrease in the $T_{50,90}$'s, with Pd/Pt(1/3)/SiO_2 @Zr (DG) achieving $T_{50,90}$'s at 153, 156 °C for CO and 171, 200 °C for THCs, respectively. Moreover, Pd/Pt(1/3)/SiO_2@Zr showed enhanced hydrothermal stability. XRD and TEM showed that in the hydrothermally aged bimetallic catalysts, the fraction of Pd present as a Pt-Pd metallic alloy increased with Pt content. The enhanced low temperature performance of Pd/Pt(1/3)/SiO_2@Zr compared to the other studied catalysts was attributed to Pd being primarily present in metallic form, despite being subjected to severe oxidizing conditions.

1. Introduction

Automobile manufacturers are required to develop efficient aftertreatment catalysts for diesel vehicles to meet the increasingly stringent emission standards [1]. Moreover, improvements in the design of diesel engines resulted in lower exhaust temperatures compared to conventional engines, demanding future aftertreatment catalysts to be active at low temperatures [2–4]. Specifically, U.S. DRIVE set a goal of eliminating 90% of vehicle hazardous emissions (hydrocarbons (HCs), CO, nitrogen oxides (NO_x)) by 150 °C (150 °C challenge) [5]. The aftertreatment system of diesel vehicles is commonly composed of a diesel oxidation catalyst (DOC), a diesel particulate filter and a selective catalytic reduction (SCR) catalyst [6–8]. Long-term usage of DOCs can lead to thermal degradation of the support and/or sintering of the active metal sites [9]. Thus, the durability of DOCs is determined by evaluating their catalytic performance after hydrothermal aging at temperatures as high as 700–800 °C [10–12]. Therefore, hydrothermally stable SiO_2(core)@Zr(shell) supports were previously developed by coating SiO_2 spheres with a Zr-based shell [13]. Pd/SiO_2@Zr catalysts were further synthesized by dispersing Pd on the Zr-based shell. Pd/SiO_2@Zr catalyst had an improved surface area (112 m^2/g) compared to Pd/ZrO_2 (24 m^2/g) after hydrothermal aging at 800 °C [14]. The hydrothermal stability of Pd/SiO_2@Zr was attributed to the formation of Si-O-Zr bonds, alleviating the formation of easily crystallized ZrO_2. Specifically, 1 wt% Pd/SiO_2@Zr was able to achieve a T_{90} (the temperature that 90% conversion was achieved) for CO at 178 °C after hydrothermal aging (800 °C/10 h, feed gas: 10% O_2, 5% H_2O, 5% CO_2/Ar), closely approaching the 150 °C challenge. However, improving the total HC (THC) conversion over Pd/SiO_2@Zr is desired, since hydrothermally aged Pd/SiO_2@Zr catalysts were only able to convert 90% of THCs at

☆ Notice: This manuscript has been authored by UT-Battelle, LLC, under Contract No. DE-AC0500OR22725 with the U.S. Department of Energy. The United States Government and the publisher, by accepting the article for publication, acknowledge that the United States Government retains a non-exclusive, paid-up, irrevocable, world-wide license to publish or reproduce the published form of this manuscript, or allow others to do so, for the United States Government purposes. The Department of Energy will provide public access to these results of federally sponsored research in accordance with the DOE Public Access Plan (http://energy.gov/downloads/doe-public-access-plan).

* Corresponding author.
E-mail address: elenikyr@buffalo.edu (E.A. Kyriakidou).

https://doi.org/10.1016/j.apcatb.2023.122436
Received 4 October 2022; Received in revised form 22 December 2022; Accepted 4 February 2023
Available online 7 February 2023

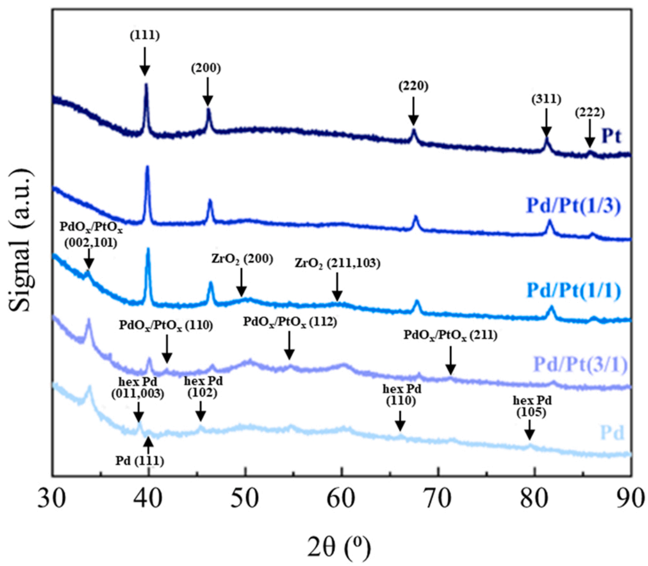

Fig. 1. XRD of hydrothermally aged Pd/SiO_2@Zr, Pd/Pt(3/1, 1/1, 1/3)/SiO_2@Zr, and Pt/SiO_2@Zr catalysts. The PdOx/PtOx phase refers to the solid solution of Pt,Pd in the tetragonal palladinite crystal structure.

temperatures as high as 382 °C.

Platinum (Pt)-based catalysts have been reported to have an improved HC oxidation activity compared to Pd-based catalyst [15–17]. Therefore, Pt attracted the interest of the emission control community for the development of catalysts that can convert HCs more efficiently compared to Pd-based catalysts to approach the 150 °C challenge. For example, Pt/Al_2O_3 was able to achieve higher C_3H_8 conversion (80% at 370 °C) than Pd/Al_2O_3 (10% at 370 °C) with the same monolith metal loading of 50 g/ft^3 [17]. In another study, Pt/Al_2O_3 was able to achieve 100% C_3H_6 conversion at 220 °C, while Pd/Al_2O_3 with the same metal loading (mol%) achieved 55% C_3H_6 conversion at 290 °C [15]. However, in a diesel oxidation reaction, where CO coexists with HCs, CO can be strongly adsorbed on the Pt surface sites of monometallic Pt-based catalysts inhibiting HC oxidation [16,18,19]. Kang et al. compared the C_2H_4 oxidation performance of Pt/Al_2O_3 in the presence and absence of CO [18]. The results indicated that C_2H_4 lights off at 220 °C and 300 °C in the absence and presence of CO, respectively, which is close to the temperature that 90% CO was converted, implying that CO poisoned the Pt sites. Moreover, monometallic Pt catalysts suffer from severe sintering because Pt is mobile due to its high volatility when exposed to temperatures greater than 800 °C [20–22]. For example, Kaneeda at al. showed that the Pt crystallite size in Pt/Al_2O_3 increased from 25 to 60 nm after exposing the catalyst to 830 °C in air for 60 h, leading to a decrease in the NO oxidation conversion from 70% to 40% at 300 °C due to the decreased surface area of active Pt. Pt sintering can be retarded by Pd incorporation by trapping mobile Pt species with PdO and/or forming Pd-Pt alloy [20,21,23]. Furthermore, metallic Pd in Pd-Pt alloys [24] is more active compared to PdO for HC oxidation [25–27]. Specifically, reduced Pd/Al_2O_3 achieved a lower T_{50} (the temperature that 50% conversion was achieved) (440 °C) compared to oxidized Pd/Al_2O_3 (T_{50} = 473 °C) for the CH_4 oxidation reaction [25].

Apart from the perspective of the catalytic performance, the rising price of Pd (Dec. 2001: $405/troy oz; Dec. 2022: $1855/troy oz) and Pt (Dec. 2001: $466/troy oz; Dec. 2022: $1019/troy oz) in the past decade requires an optimization of Pd and Pt usage in DOC applications [28]. Herein, a series of Pd/Pt bimetallic DOCs with Pd/Pt molar ratios varying from 1/3–3/1 were synthesized using hydrothermally stable SiO_2@Zr support. Monometallic Pd/SiO_2 @Zr and Pt/SiO_2@Zr catalysts were also prepared for comparison purposes. The synthesized catalysts were evaluated for their low temperature diesel oxidation activity and hydrothermal stability using the low temperature aftertreatment protocol developed by U.S. DRIVE [10]. Evaluation results suggested that the degreened Pd/Pt(1/3)/SiO_2@Zr showed the best performance among the studied catalysts with different Pd/Pt molar ratios, with the lowest $T_{50,90}$'s at 153, 156 °C for CO and 171, 200 °C for THCs. Moreover, bimetallic Pd/Pt(1/3)/SiO_2@Zr exhibited retainable performance after hydrothermal aging treatment. Characterization results suggested that decreasing the Pd/Pt molar ratio from 3/1–1/3 led to an increase in the fraction of Pd that was alloyed with Pt in the metallic portion of the catalyst. Specifically, decreased peak areas attributed to the oxide phase Pd,Pt (H_2-temperature programmed reduction (TPR)) and higher intensity of metallic phase (X-ray diffraction (XRD)) was observed. Moreover, transmission electron microscopy (TEM) suggested that a decrease in Pd/Pt molar ratio from 3/1–1/3 led to an increase in the Pd and Pt percentage in the metallic phase from 50% to 68%, and 50–69%, respectively.

2. Experimental

2.1. Reagents and materials

Zirconium(IV) butoxide solution (Zr(BuO)$_4$) (80 wt.% in 1-butanol, Sigma-Aldrich), tetraethyl orthosilicate (TEOS) (98% purity, Strem), anhydrous ethanol (EtOH, 200 proof, Decon), ammonium hydroxide (NH_4OH, 28–30 wt.% solution of NH_3 in water, Sigma-Aldrich), tetraamminepalladium nitrate ($Pd(NH_3)_4(NO_3)_2$) (10% in H_2O, Sigma-Aldrich) and tetraammineplatinum nitrate ($Pt(NH_3)_4(NO_3)_2$) (99% purity, Strem) were used as received. A 3.76 wt.% aqueous solution of Brij30 ($C_{12}H_{25}(OCH_2CH_2)_4OH$) (ACROS) was prepared prior to usage. DI water with a resistivity of 18.2 MΩ•cm was used for all the synthesis performed in this study.

2.2. Synthesis of SiO_2(core)@Zr(shell) supports

SiO_2@Zr supports were synthesized using a previously reported synthesis method [13,29]. Briefly, monodisperse SiO_2 spheres were prepared following the Stöber method [29]. Specifically, 172 mL EtOH, 10.8 mL DI water and 4.43 mL NH_4OH were mixed for 10 min, followed by the addition of 12.5 mL TEOS. The obtained solution was stirred overnight at room temperature (RT). The liquid phase of the obtained mixture was exchanged by EtOH (200 mL) and 200 mL DI water (3 times) followed by another exchange with 200 mL EtOH (3 times) by centrifugation (5000 rpm). The obtained SiO_2 spheres were suspended in 200 g EtOH followed by the addition of 1 mL of Brij30 solution and the suspended solution was stirred for 1 h at RT. 3.6 mL Zr(BuO)$_4$ was then added to the suspended solution that was stirred overnight at RT. The liquid phase of the obtained mixture was then separated and exchanged for 200 mL DI water and the final mixture was aged at RT for 3 days. The SiO_2@Zr support was collected by centrifugation (5000 rpm), followed by drying at 110 °C overnight and calcination at 500 °C for 2 h (ramp rate = 10 °C/min).

2.3. Catalyst preparation

Monometallic 1 wt.% Pd/SiO_2@Zr and 1.8 wt.% Pt/SiO_2@Zr catalysts were prepared by a wet-impregnation method using 4.7 × 10^{-3} M $Pd(NH_3)_4(NO_3)_2$ and 4.7 × 10^{-3} M $Pt(NH_3)_4(NO_3)_2$ stock solutions. Specifically, 20 mL of Pd and Pt stock solution was added to 1 g SiO_2@Zr resulting to 1 wt.% Pd/SiO_2@Zr and 1.8 wt.% Pt/SiO_2@Zr, respectively. 1.8 wt.% Pt/SiO_2@Zr contains the same moles of precious metal as 1 wt.% Pd/SiO_2@Zr. The greater metal weight loading of 1.8 wt.% Pt/SiO_2@Zr compared to 1 wt.% Pd/SiO_2@Zr is attributed to the greater atomic mass of Pt (195.1 au) compared to Pd (106.4 au). Bimetallic Pd/Pt/SiO_2@Zr catalysts with Pd/Pt molar ratios of 1/3, 1/1 and 3/1 were prepared by co-impregnation where calculated amounts of 4.7 × 10^{-3} M $Pd(NH_3)_4(NO_3)_2$ and 4.7 × 10^{-3} M $Pt(NH_3)_4(NO_3)_2$ were premixed and added to 1 g of SiO_2@Zr (20 mL stock solution to 1 g support, with

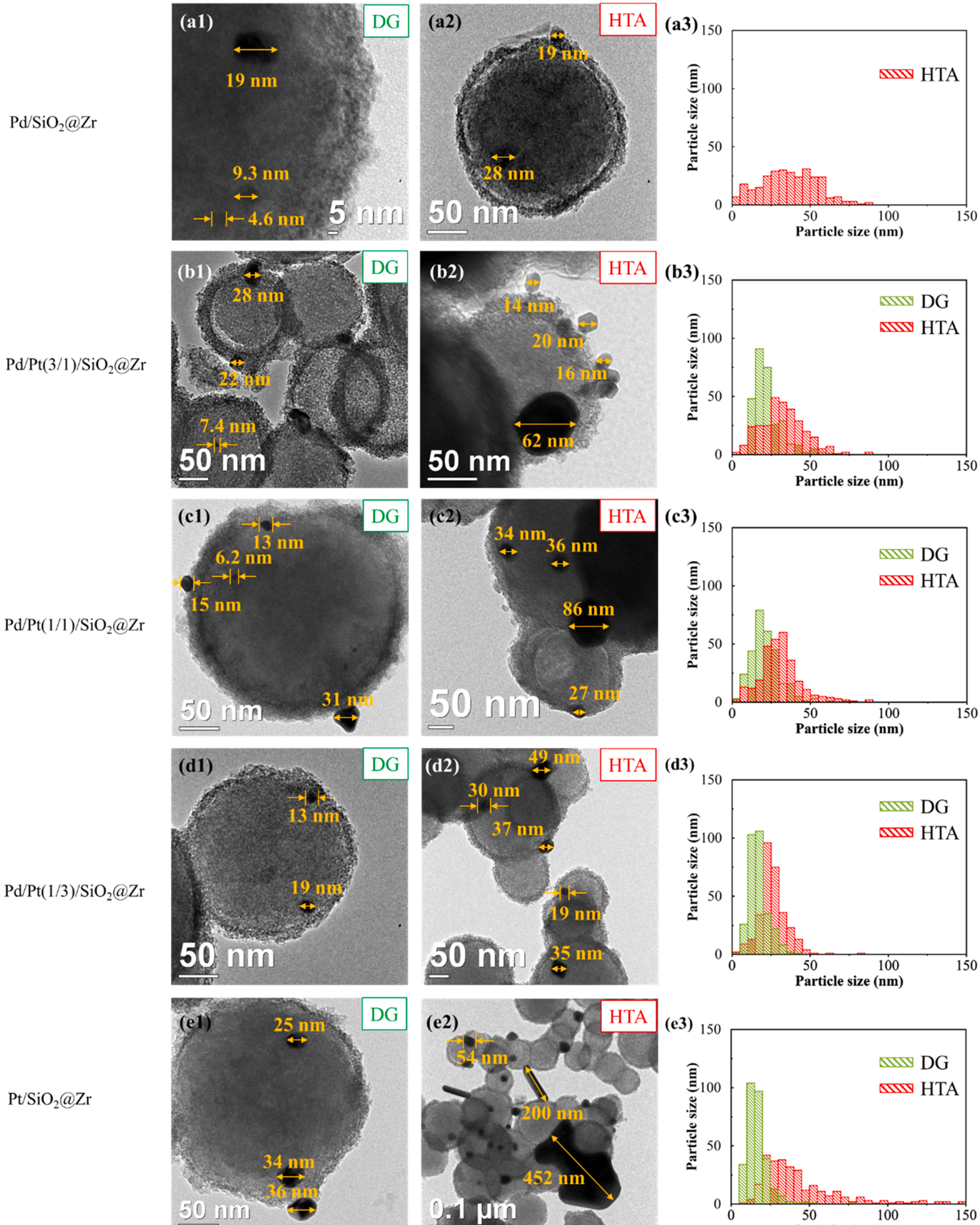

Fig. 2. (a-e) (1,2) TEM images and (a-e) (3) particle size distributions of DG and HTA (a) Pd/SiO$_2$@Zr, (b) Pd/Pt(3/1)/SiO$_2$@Zr, (c) Pd/Pt(1/1)/SiO$_2$@Zr, (d) Pd/Pt (1/3)/SiO$_2$@Zr, and (e) Pt/SiO$_2$@Zr catalysts.

Table 1
Pd, Pt particle sizes of DG and HTA catalysts determined by TEM.

Sample	DG	HTA
Pd/SiO_2 @Zr	-	23.0 (σ = 7.2)
$Pd/Pt(3/1)/SiO_2$ @Zr	31.1 (σ = 9.5)	50.4 (σ = 16.2)
$Pd/Pt(1/1)/SiO_2$ @Zr	32.3 (σ = 10.1)	58.6 (σ = 18.3)
$Pd/Pt(1/3)/SiO_2$ @Zr	21.3 (σ = 6.1)	32.4 (σ = 8.9)
Pt/SiO_2 @Zr	25.8 (σ = 7.5)	78.7 (σ = 25.9)[a]

[a] only particles smaller than 150 nm were taken into consideration, hence the actual particle size is underestimated.

1/3, 1/1 and 3/1 (v/v) of Pd/Pt stock solution). All synthesized bimetallic $Pd/Pt/SiO_2$@Zr catalysts had the same total moles of precious metal as the 1 wt.% Pd/SiO_2@Zr (Table S1). The liquid phase used for wet impregnation was evaporated with rigorous stirring at RT, followed by drying at 110 °C overnight and calcination at 500 °C for 2 h (ramp rate = 10 °C/min).

2.4. Characterization

The morphology of the SiO_2@Zr support and the particle size determination of the active metals were obtained by TEM (JEM-2010 F) at an accelerating voltage of 200 kV. Higher resolution images were also obtained with an aberration corrected TEM/scanning transmission electron microscopy (STEM) instrument (JEOL NeoARM). Energy dispersive X-ray spectroscopy (EDS) mapping and analysis was performed using an Oxford Aztec 3.0 system. The catalysts were initially dispersed in ethanol under ultrasonication before imaging. The suspended catalyst was then added drop wisely onto a carbon-coated copper TEM grid (Electron Microscopy Sciences, CF300-CU) followed by drying in air at RT.

2D-XRD patterns were obtained on a Rigaku D/Max instrument equipped with CoKα radiation source (λ = 1.78899 Å, 40 kV, 30 mA), a 0.8 mm collimator, and a Fe filter. As synthesized samples were mounted perpendicularly to the goniometer using a sample stage fabricated in house and patterns were collected for 6 h. 2θ scans were collected using a Rigaku SmartLab diffractometer equipped with a Cu-Kα X-ray source (40 kV, 40 mA), a D/TEX detector, and a Ni filter. As synthesized samples were mounted on a low background quartz sample holder and patterns were collected for 2.5 h.

H_2-TPR experiments were conducted in a Micromeritics AutoChem II 2920 device equipped with a thermal conductivity detector (TCD). 50 mg of sample was loaded in a U-shaped quartz tube reactor stabilized by packed quartz wool and a total flow rate of 50 sccm (mL/min (STP)) was applied. The samples were initially pretreated with 20% O_2/Ar at 500 °C for 30 mins prior to the H_2-TPR measurements. The samples were initially cooled down to − 50 °C (isopropyl alcohol and liquid nitrogen mixture) in Ar and the TCD signal was stabilized before further measurements. The samples were then heated to 400 °C (10 °C/min) in 10% H_2/Ar while the TCD signal was recorded.

2.5. Catalyst evaluation

Catalyst evaluation was performed in a customized fixed-bed U-shaped quartz reactor as reported previously [30]. The reactor was placed in a cylindrical furnace surrounded by quartz wool to eliminate heat gradients. Catalyst powders were pressed and sieved into pellets with sizes ranging from 250 to 500 μm to eliminate pressure effects during reaction. 100 mg of catalyst pellets was placed in the U-tube reactor supported by two quartz wool plugs. The furnace temperature, controlled with a PID temperature controller, and the inlet gas temperature were measured by K-type thermocouples placed outside and inside the U-shaped reactor, respectively, close to the upper plug of quartz wool. Water was supplied by a D-series syringe pump (Teledyne Isco) to a tube furnace (200 °C) where it got evaporated and steam was carried in the reactor by Ar. All gas lines after water introduction were heated to 170 °C to avoid water condensation. The reactor exhaust was diluted with 667 sccm Ar and analyzed by an MKS MultiGas 2030 FTIR gas analyzer operating at 191 °C.

The catalysts were initially pretreated at 600 °C for 20 min in 12% O_2, 6% H_2O, 6% CO_2/Ar and they were evaluated after degreening (DG) (700 °C/4 h) and hydrothermal aging (HTA) (800 °C/10 h) under the flow of 10% O_2, 5% H_2O, 5% CO_2/Ar. Simulated diesel oxidation experiments were performed using the low temperature combustion of diesel (LTC-D) gas composition defined by U.S. DRIVE (12% O_2, 6% H_2O, 6% CO_2, 400 ppm H_2, 2000 ppm CO, 100 ppm NO, 250 ppm C_2H_4, 100 ppm C_3H_6, 33 ppm C_3H_8, 210 ppm n-$C_{10}H_{22}$/Ar (HCs in C_1 basis)) [10]. Diesel oxidation experiments were conducted from 100 to 500 °C with a ramp rate of 2 °C/min. The total flow rate was 333 sccm, corresponding to a gas hourly space velocity (GHSV) of 113,000 h^{-1}. A set of MKS mass flow controllers were used to regulate the flows of CO_2, O_2, H_2, CO, NO, C_2H_4, C_3H_6, C_3H_8, and Ar (99.999% UHP, Airgas). Liquid n-$C_{10}H_{22}$ was placed in a bubbler immersed in a water bath maintained at 20 °C and it was carried in the reactor by Ar. The flow of Ar required to carry the desired amount of n-$C_{10}H_{22}$ was calculated with the Clausius-Clapeyron equation using the vapor pressure of n-$C_{10}H_{22}$ at 20 °C (0.16 kPa) [31].

3. Results and discussion

3.1. Catalyst characterization

3.1.1. XRD analysis

XRD was performed on hydrothermally aged Pd/SiO_2@Zr, Pd/Pt(3/1, 1/1, 1/3)/SiO_2@Zr, and Pt/SiO_2@Zr catalysts (Fig. 1). The peaks corresponding to the fcc metallic phase are well defined in the Pt and Pd/Pt catalysts, and the peak positions are consistent with the literature [32,33]. The peaks are shifted to lower angles with increasing Pt content from $Pd/Pt(3/1)/SiO_2$@Zr to Pt/SiO_2@Zr. Such a peak shift is attributed to the expansion of the lattice with increasing Pt content, consistent with the larger atomic radius of Pt (1.77 Å) compared to Pd (1.69 Å) [34,35]. The peak position is used to estimate the composition of the metallic Pd/Pt particles using Vegard's law [36], assuming a linear relationship between the lattice parameters of Pd (3.8898 Å) [37] and Pt (3.9231 Å) [38]. Specifically, HTA $Pd/Pt(3/1)/SiO_2$@Zr was calculated to have a lower Pd/Pt weight ratio (Pd/Pt = 44/56) than the bulk catalyst (Pd/Pt = 63/37) (Table S1). This is due to a portion of Pd being present as an oxide, leading to Pd-dominated Pd-Pt oxide particles over HTA Pd/Pt (3/1)/SiO_2@Zr as confirmed by the XRD peaks of the tetragonal oxide phase [39,40]. For the HTA $Pd/Pt(1/1)/SiO_2$@Zr catalyst, the Pd/Pt weight ratio for the metallic phase obtained from XRD (39/61) was similar to the nominal Pd/Pt weight ratio (36/64) suggesting that Pd and Pt are uniformly dispersed in both oxide and metallic phases. Finally, the Pd/Pt weight ratio obtained from XRD for the metallic portions of the HTA $Pd/Pt(1/3)/SiO_2$@Zr (24/76) was slightly greater than the bulk Pd/Pt weight ratio (14/86). This observation can be attributed to the existence of Pt-rich Pd-Pt alloy along with metallic phases of Pt and Pd. However, the presence of such phases is beyond the detection limits of XRD. A more detailed discussion of Pd-Pt alloy, oxide and metallic phases of Pd and Pt is provided later in this section. The HTA Pd/SiO_2@Zr catalyst shows primarily the oxide phase, with small peaks from hex Pd [41]. In contrast, the Pd is present as a Pt-Pd alloy in the bimetallic catalysts, with the fraction of Pd present in metallic form increasing with Pt content.

3.1.2. TEM-EDS analysis

The average particle size of all degreened and hydrothermal aged catalysts was determined by TEM. Representative micrographs and particle size distributions of all studied samples are shown in Fig. 2 and S1. The size of at least 300 particles was taken into consideration when calculating the Sauter mean diameter (d_{32}) [42] (Table 1). Few particles

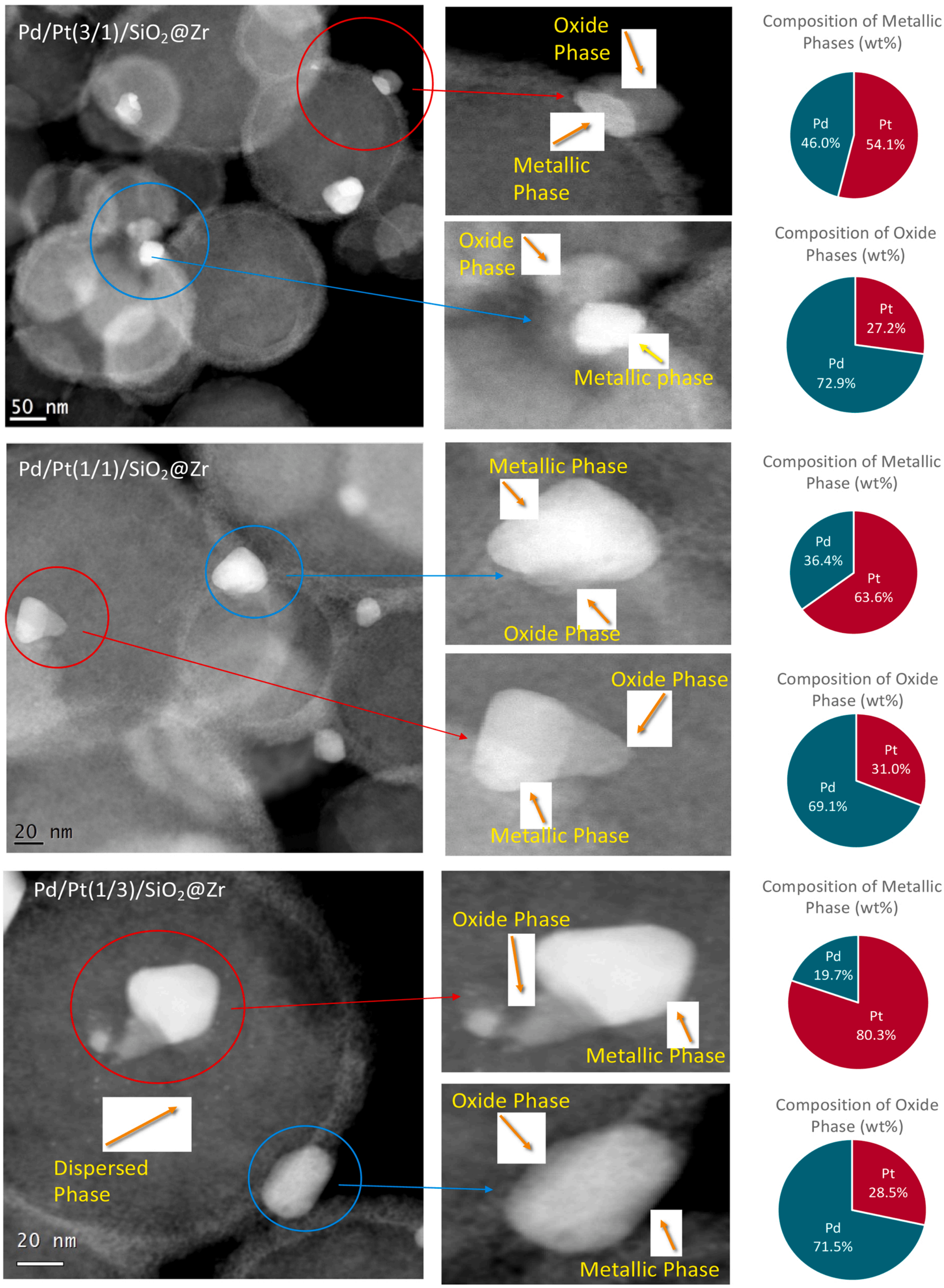

Fig. 3. TEM images of hydrothermally aged (a) Pd/Pt(1/3)/SiO_2@Zr, (b) Pd/Pt(1/1)/SiO_2@Zr, and (b) Pd/Pt(3/1)/SiO_2@Zr catalysts showing the presence of oxide and metallic phases co-existing in individual particles, and their composition determined by EDS analysis.

were observed from DG Pd/SiO_2@Zr consistent with the broad XRD peaks seen in Fig. 1. It is noted that due to the close atomic mass between Pd (106.42 u) and Zr (91.224 u), small Pd particles in Pd-containing catalysts may not be distinguishable in the TEM images. Other DG catalysts showed similar average particle sizes of ~20–30 nm. HTA at 800 °C resulted in a 52–203% increase in the particle size of all studied catalysts compared to their DG states. Large, non-spherical particle aggregates (17 out of 310 measured particles) with particle sizes varying from 150 to 452 nm were observed over HTA Pt/SiO_2@Zr and they were not taken into consideration when determining the Sauter mean

Table 2
Pd, Pt composition (wt.%) of the metallic portion of the biphasic particles of HTA Pd/Pt(3/1)/SiO_2@Zr, Pd/Pt(1/1)/SiO_2@Zr, and Pd/Pt(1/3)/SiO_2@Zr catalysts as inferred from XRD (Vegard's law) and TEM-EDS and the nominal composition of these catalysts. The deviations indicate the presence of both Pt and Pd in the oxide phase.

Sample	Composition (wt%)					
	XRD		EDS		Nominal	
	Pd	Pt	Pd	Pt	Pd	Pt
Pd/Pt(3/1)/SiO_2@Zr	44	56	46	54	63	38
Pd/Pt(1/1)/SiO_2@Zr	39	61	36	64	36	64
Pd/Pt(1/3)/SiO_2@Zr	24	76	20	80	16	84

diameter. The formation of abnormally large particles is attributed to the high mobility of Pt at elevated temperature [18,43]. Pd-containing catalysts showed relatively smaller particle sizes (d_{32} = 23.0–58.6 nm) compared to Pt/SiO_2@Zr (78.7 nm). This behavior can be attributed to the low vapor pressure and mobility of the PdO phase and its ability to trap mobile PtO_2 during hydrothermal aging that can slow down Pt sintering [21,44]. Overall, all catalysts showed a broad particle size distribution (standard deviation of 9–26 nm), with severe sintering seen in HTA Pt/SiO_2@Zr.

The lattice fringes in the TEM images were analyzed using fast Fourier transforms (FFT) allowed indexing of the phases in HTA Pd/SiO_2@Zr catalysts. Fig. S2(a-c (1,2)) shows the TEM images for HTA Pd/SiO_2@Zr. FFT patterns of the yellow boxed regions show lattice fringes that are consistent with tetragonal PdO. TEM images of all HTA bimetallic Pd/Pt/SiO_2@Zr catalysts were also collected (Fig. 3) and the phases were confirmed by analyzing the lattice fringes. In all cases, the metallic component was consistent with the fcc Pt-Pd alloy and the oxide phase was tetragonal containing both Pt and Pd, implying that Pt was present as a solid solution in PdO. The bimetallic catalysts contained particles that were biphasic, containing a metallic (bright, in dark field images) phase adjacent to an oxide phase (grey, in dark field images). Similar conclusion regarding the occurrence of Pd and Pt uniformly dispersed in both oxide and metallic phases were also drawn from the XRD results for HTA Pd/Pt(1/1)/SiO_2@Zr. The composition of the oxide and metallic phases in individual biphasic particles was analyzed and the average is reported in Fig. 3 and S3. Moreover, a dispersed phase (particles < 10 nm) was also observed in HTA Pd/Pt(1/1)/SiO_2@Zr and Pd/Pt(1/3)/SiO_2@Zr as shown in Fig. S4. It is seen that the oxide phase is always Pd rich, as expected from the stability of the tetragonal PdO phase, but surprisingly, there is Pt present in this oxide phase, presumably as a solid solution. Since the ionic sizes of Pt and Pd are similar, and both prefer the square planar structure, it is likely that this solid solution is stable at these high temperatures. To our knowledge, this solid solution of Pt in PdO has not been reported previously. Regarding the metallic phase, it is seen from Fig. 3 that as the Pt content is increased, the composition of the alloy becomes Pt-rich. It is significant that while Pd under these conditions would be present only as an oxide, in these bimetallic catalysts, Pd is present both in metallic and oxide form. The composition of the metallic phase determined by TEM-EDS is consistent with the XRD analysis using the lattice constant and Vegard's law (Table 2).

The TEM-EDS data on individual nanoparticles in Fig. 3 was combined to generate the overall speciation for Pt and Pd into oxide and metallic phases, as shown in Fig. 4. It is evident from Fig. 4 that the amount of Pd and Pt present in the metallic phase of the biphasic particles increased from 50 wt.% Pd and 50 wt.% Pt over HTA Pd/Pt(3/1)/SiO_2@Zr to 68 wt.% Pd and 69 wt.% Pt over HTA Pd/Pt(1/3)/SiO_2@Zr. Further, EDS elemental analysis of the oxide phase of the biphasic particles suggested that apart from Pd, Pt was also present in oxide phase (Figs. 3 and 4). A possible explanation of this behavior is that Pt diffusion into the PdO lattice, can create a Pd, Pt solid solution that can retard the sintering of Pt observed in HTA Pt/SiO_2@Zr (Table 1 and Fig. 2). Pd/Pt biphasic particles were previously reported to consist of a Pd/Pt alloy phase adjacent to a PdO phase [21,45]. The formation of the PdO phase was attributed to the low surface energy of Pd compared to Pt and its tendency to segregate from the Pd/Pt alloy. Here we show that the oxide and metal phases co-exist in individual particles, and report for the first time the observation of a Pt/Pd solid solution in the oxide phase of biphasic particles.

3.1.3. H_2-TPR analysis

The H_2-TPR (Fig. 5) provides further evidence of the speciation of Pd, Pt into metallic and oxide phases. Table S2 provides the areas of the H_2-TPR peaks at temperatures below RT over the studied samples. The fresh catalysts were calcined at 500 °C in air. The Pd-only catalyst was present as an oxide and showed two distinct peaks and a broad peak which might arise from a dispersed PdO phase. The peak at 6 °C is attributed to the reduction of PdO to metallic Pd and the formation of palladium hydride (PdH_x) [17,46,47]. PdH_x decomposes at higher temperatures resulting in a negative peak at 70 °C [48]. The H_2-TPR data for the HTA Pd/SiO_2@Zr sample is very similar to that of the fresh catalyst, indicating similar speciation. In contrast, no reduction peaks were observed over fresh and HTA Pt/SiO_2@Zr, suggesting that Pt is present in metallic form, which is consistent with the Pt oxides not being stable at elevated temperatures [49]. The Pd and Pt speciation in the monometallic catalysts is consistent with the XRD data, showing a broad Pd oxide peak and a sharp Pt metallic peak.

In contrast to the Pd-only catalyst, the fresh bimetallic catalysts show very small peaks during H_2-TPR indicating that these catalysts are largely metallic and that Pt helps to retain Pd in metallic form in the fresh catalysts. A large H_2-TPR peak was observed over the HTA catalysts, indicating the presence of an oxide phase, as also shown by TEM-EDS. The HTA bimetallic catalysts show H_2-TPR peaks, and the H_2 consumption at temperatures below RT (Table S2) is used as a measure of the oxide content after HTA. Compared to HTA Pd/SiO_2@Zr (35.8 μmol/g), the HTA bimetallic Pd/Pt/SiO_2@Zr catalysts showed significant H_2 consumption (52.7 μmol/g (Pd/Pt(3/1)/SiO_2@Zr), 27.7 μmol/g (Pd/Pt(1/1)/SiO_2@Zr) and 2.4 μmol/g (Pd/Pt(1/3)/SiO_2@Zr)) despite the progressively lower amounts of Pd in these catalysts. This occurs over the HTA bimetallic Pd/Pt/SiO_2@Zr catalysts due to trapping of volatile PtO_2 by the PdO phase [21,50]. The increased H_2 consumption observed after HTA over the studied bimetallic catalysts is therefore consistent with Pt being present as an oxide in these catalysts, in the form of biphasic particles as shown via TEM-EDS in Figs. 3 and 4. The H_2-TPR data clearly shows that the Pd/Pt(1/3)/SiO_2@Zr catalyst is largely metallic, consistent with the TEM images.

3.2. Activity test results

The catalytic performance of DG Pd/SiO_2@Zr, Pd/Pt(3/1)/SiO_2@Zr, Pd/Pt(1/1)/SiO_2@Zr, Pd/Pt(1/3)/SiO_2@Zr, and Pt/SiO_2@Zr catalysts is shown in Fig. 6 and S5. The CO/THC T_{50} and T_{90} for DG Pd/SiO_2@Zr was at 176/223 °C and 186/291 °C, respectively. The replacement of 25% Pd by Pt (Pd/Pt(3/1)/SiO_2 @Zr) resulted in a decrease in the T_{50}/T_{90} at 166/169 °C (CO) and 198/244 °C (THC). The performance of Pd/Pt/SiO_2@Zr further improved when the Pd/Pt molar ratio decreased to 1/1 and 1/3, as indicated by a decrease in T_{50}/T_{90} for CO to 160/165 °C and 153/156 °C, respectively. The THC T_{50}/T_{90} also decreased with decreasing Pd/Pt molar ratio from 3/1–1/1 (T_{50}/T_{90} = 182/229 °C) to 1/3 (T_{50}/T_{90} = 171/200 °C). Moreover, NO_x conversions (Fig. S5) increased with decreasing Pd/Pt molar ratio. This behavior can be attributed to NO_x undergoing a HC-SCR reaction where Pt was reported to be more active compared to Pd [51]. While the THC T_{50}/T_{90} = 181/193 °C over monometallic DG Pt/SiO_2@Zr were achieved at relative low temperatures, the $T_{50,90}$'s for CO increased to 180 and 184 °C, respectively, compared to bimetallic Pd/Pt catalysts. These CO $T_{50,90}$'s were close to the light-off temperature (T_{10}) of THCs at 180 °C, implying the occurrence of CO poisoning on the active Pt sites [16,18].

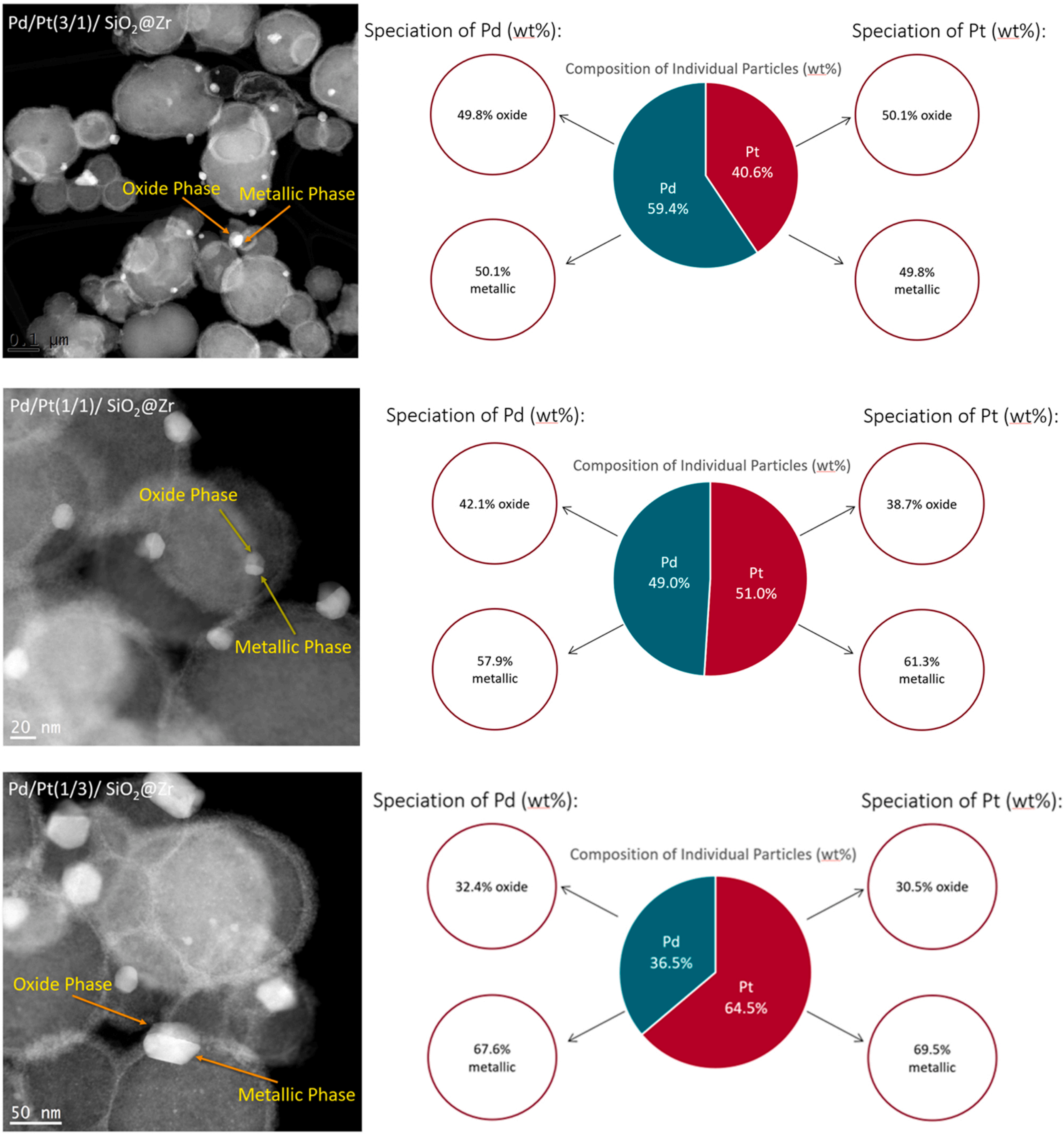

Fig. 4. Speciation of Pt and Pd as detected by EDS analysis of individual particles into oxide and metallic phases. It is evident that with increasing Pt content, more of the Pd is present in metallic form. In all samples, a significant fraction of Pt is present in oxide form, as a solid solution in the PdO tetragonal lattice.

The performance of all studied catalysts after HTA is shown in Fig. 7 and S6. All studied catalysts deactivated after hydrothermal aging, as indicated by an increase in the T_{50}/T_{90} of CO and THCs compared to the DG state of the catalysts (Fig. 7(c,d)). HTA Pd/Pt(1/3)/SiO_2@Zr outperformed all studied catalysts with T_{50}/T_{90} of 159/163 °C for CO and 170/213 °C for THCs, respectively. Thus, the improved CO and THC oxidation performance of Pd/Pt(1/3)/SiO_2@Zr can be attributed to the increased metallic phase in the biphasic particles [25–27]. Again, HTA Pt/SiO_2@Zr performed T_{50} for THC conversion at 192 °C, close to the CO T_{50} at 191 °C, due to the CO poisoning. In a nutshell, the improved CO and THC oxidation performance of the bimetallic Pd/Pt compared to monometallic catalysts is due to the increase in Pd and Pt content in the metallic phase of biphasic particles with a decrease in Pd/Pt molar ratio.

4. Conclusions

A simulated LTC-D gas mixture (feed: 6% CO_2, 12% O_2, 6% H_2O, 400 ppm H_2, 2000 ppm CO, 100 ppm NO, 500 ppm C_2H_4, 300 ppm C_3H_6, 100 ppm C_3H_8, 2100 ppm n-$C_{10}H_{22}$; HCs in C_1 basis and GHSV = 113,000 h^{-1}) was applied for the DOC evaluation of a series of mono- and bi-metallic Pd/Pt/SiO_2@Zr catalysts. DG Pd/Pt(1/3)/ SiO_2@Zr outperformed all studied DG catalysts (T_{90} (CO) = 156 °C, T_{90} (THCs) = 200 °C), approaching the 150 °C challenge. HTA Pd/Pt/ SiO_2@Zr catalysts showed only a slight deactivation compared to their DG states, suggesting that the studied bimetallic studied catalysts are hydrothermally stable. Biphasic particles were observed over HTA aged bimetallic Pd/Pt/SiO_2@Zr catalysts. An increased percentage of Pd, Pt

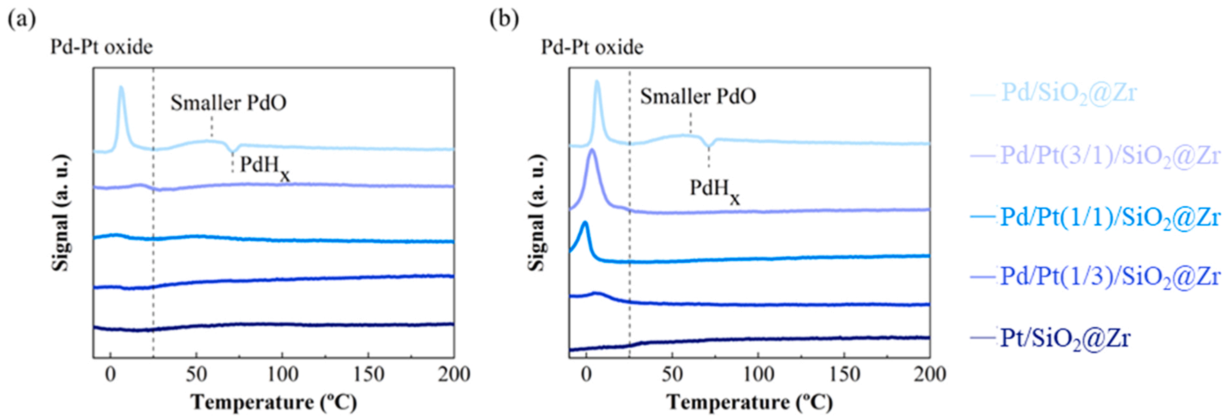

Fig. 5. H_2-TPR of (a) fresh and (b) HTA Pd/SiO_2@Zr, Pd/Pt(3/1)/SiO_2@Zr, Pd/Pt(1/1)/SiO_2@Zr, Pd/Pt(1/3)/SiO_2@Zr, and Pt/SiO_2@Zr catalysts.

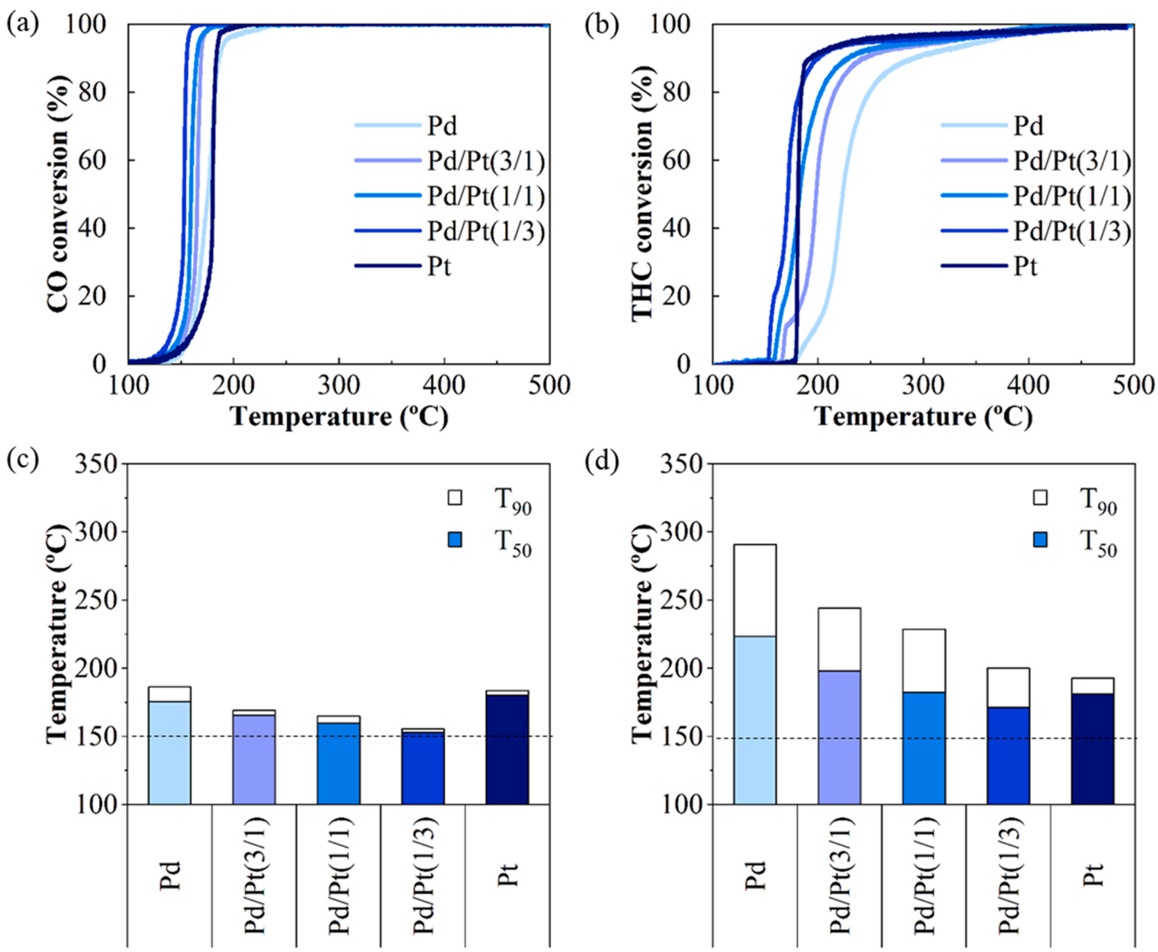

Fig. 6. (a) CO and (b) THC conversion and $T_{50,90}$'s of (c) CO and (d) THCs over degreened Pd/SiO_2@Zr, Pd/Pt(1/3)/SiO_2@Zr, Pd/Pt(1/1)/SiO_2@Zr, Pd/Pt(1/3)/SiO_2@Zr, and Pt/SiO_2@Zr catalysts.

are present in the metallic phase of the biphasic particles as the Pd/Pt molar ratio decreased from 3/1, 1/1, to 1/3, which can contribute to the improved HC oxidation performance of HTA Pd/Pt(1/3)/SiO_2@Zr. Furthermore, Pt can be trapped by PdO in the biphasic particles that can retard Pt sintering. Overall, this work highlights the potential use of bimetallic Pd/Pt/SiO_2@Zr catalysts as DOCs and it reveals that an improved performance can be achieved by decreasing the Pd/Pt molar ratio to increase the Pd and Pt content in the metallic phase of biphasic particles.

CRediT authorship contribution statement

Chih-Han Liu: Conceptualization, Methodology, Validation, Formal analysis, Investigation, Writing – original draft, writing – review & editing, Visualization, **Stephen Porter:** Formal analysis, Investigation, Writing – original draft, Visualization, **Junjie Chen:** Conceptualization, Methodology, Investigation, Writing – review & editing, **Hien Pham:** Formal analysis, Investigation, Writing – moriginal draft, Visualization, **Eric J. Peterson:** Methodology, Formal analysis, Investigation, **Prateek**

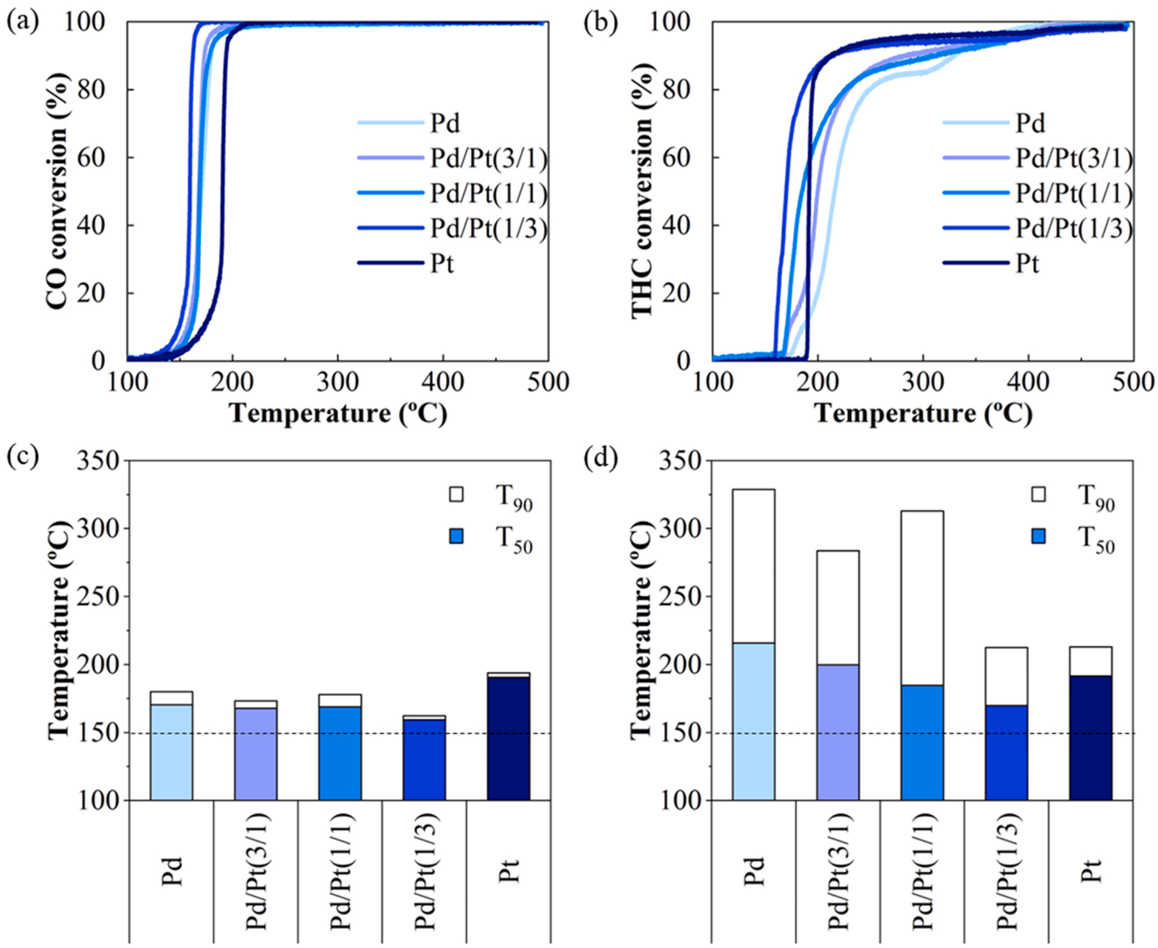

Fig. 7. (a) CO and (b) THC conversion and $T_{50,90}$'s of (c) CO and (d) THCs over hydrothermally aged Pd/SiO_2@Zr, Pd/Pt(1/3)/SiO_2@Zr, Pd/Pt(1/1)/SiO_2@Zr, Pd/Pt (1/3)/SiO_2@Zr, and Pt/SiO_2@Zr catalysts.

Khatri: Writing – review & editing, **Todd J. Toops:** Conceptualization, Supervision, Writing – review & editing. **Abhaya Datye:** Conceptualization, Resources, Writing – review & editing, **Eleni A. Kyriakidou:** Conceptualization, Resources, Writing – review & editing, Supervision, Funding acquisition.

Declaration of Competing Interest

The authors declare that they have no known competing financial interests or personal relationships that could have appeared to influence the work reported in this paper.

Data Availability

Data will be made available on request.

Acknowledgements

Financial support for the catalyst characterization via TEM was provided by the U.S. Department of Energy (DOE)/BES Catalysis Science program, grant DE-FG02-05ER15712. Additional support was provided by the DOE Energy Efficiency and Renewable Energy (EERE), Vehicle Technologies Office (DE-FOA-0002197). Acquisition of the TEM was supported by the NSF MRI grant DMR-1828731.

Appendix A. Supporting information

Supplementary data associated with this article can be found in the online version at doi:10.1016/j.apcatb.2023.122436.

References

[1] F. Posada, S. Chambliss, K. Blumberg, Costs of emission reduction technologies for heavy-duty diesel vehicles, ICCT White paper 2016.https://theicct.org/wp-content/uploads/2021/06/ICCT_costs-emission-reduction-tech-HDV_20160229.pdf.

[2] J. Lee, J.R. Theis, E.A. Kyriakidou, Vehicle emissions trapping materials: successes, challenges, and the path forward, Appl. Catal. B Environ. 243 (2019) 397–414, https://doi.org/10.1016/j.apcatb.2018.10.069.

[3] A.P. Wong, E.A. Kyriakidou, T.J. Toops, J.R. Regalbuto, The catalytic behavior of precisely synthesized Pt–Pd bimetallic catalysts for use as diesel oxidation catalysts, Catal. Today 267 (2016) 145–156, https://doi.org/10.1016/j.cattod.2016.02.011.

[4] E.A. Kyriakidou, T.J. Toops, J.-S. Choi, M.J. Lance, J.E. Parks II, Exhaust treatment catalysts with enhanced hydrothermal stability and low-temperature activity, US Patents 10,42,137 B2 (October 1, 2019). https://patents.google.com/patent/US10427137B2/en.

[5] M. Zammit, C.L. DiMaggio, C.H. Kim, C. Lambert, G.G. Muntean, C.H. Peden, J.E. Parks, K. Howden, Future automotive aftertreatment solutions: The 150 °C challenge workshop report (US Drive Workshop, 2012). https://www.pnnl.gov/main/publications/external/technical_Reports/PNNL-22815.pdf.

[6] Y. Shin, Y. Jung, C.P. Cho, Y.D. Pyo, J. Jang, G. Kim, T.M. Kim, NO_x abatement and N_2O formation over urea-SCR systems with zeolite supported Fe and Cu catalysts in a nonroad diesel engine, Chem. Eng. J. 381 (2020), 122751, https://doi.org/10.1016/j.cej.2019.122751.

[7] B. Apicella, E. Mancaruso, C. Russo, A. Tregrossi, M.M. Oliano, A. Ciajolo, B. M. Vaglieco, Effect of after-treatment systems on particulate matter emissions in diesel engine exhaust exp, Therm. Fluid Sci. (2020), 110107, https://doi.org/10.1016/j.expthermflusci.2020.110107.

[8] A. Ko, Y. Woo, J. Jang, Y. Jung, Y. Pyo, H. Jo, O. Lim, Y.J. Lee, Complementary effects between NO oxidation of DPF and NO_2 decomposition of SCR in light-duty diesel engine, J. Ind. Eng. Chem. 80 (2019) 160–170, https://doi.org/10.1016/j.jiec.2019.07.045.

[9] C.H. Bartholomew, Mechanisms of catalyst deactivation, Appl. Catal. A Gen. 212 (2001) 17–60, https://doi.org/10.1016/S0926-860X(00)00843-7.
[10] K.G. Rappé, C. DiMaggio, J.A. Pihl, J.R. Theis, S.H. Oh, G.B. Fisher, J. Parks, V. G. Easterling, M. Yang, M.L. Stewart, Aftertreatment protocols for catalyst characterization and performance evaluation: low-temperature oxidation, storage, three-way, and NH_3-SCR catalyst test protocols, Emission Contr. Sci. Technol. 5 (2019) 183–214, https://doi.org/10.1007/s40825-019-00120-7.
[11] X.L.Wenxiang Tanga, Fangyuan Liua, Shoucheng Dua, Junfei Wenga, Son Hoanga, Sibo Wanga, Chang-Yong Namb, Pu-Xian Gaoa, Ceria-based nanoflake arrays integrated on 3D cordierite honeycombs for efficient low-temperature diesel oxidation catalyst, Appl. Catal. B Environ. 245 (2019) 623–634, https://doi.org/10.1016/j.apcatb.2019.01.028.
[12] P. Anguita, F. Gaillard, E. Iojoiu, S. Gil, A. Giroir-Fendler, Study of hydrothermal aging impact on Na-and P-modified diesel oxidation catalyst (DOC), J. Catal. 375 (2019) 329–338, https://doi.org/10.1016/j.jcat.2019.06.028.
[13] C.-H. Liu, J. Chen, T.J. Toops, J.-S. Choi, C. Thomas, M.J. Lance, E.A. Kyriakidou, Hydrothermally stable Pd/SiO_2@Zr Core@Shell catalysts for diesel oxidation applications, Chem. Eng. J. (2021), 130637, https://doi.org/10.1016/j.cej.2021.130637.
[14] M.-Y. Kim, E.A. Kyriakidou, J.-S. Choi, T.J. Toops, A.J. Binder, C. Thomas, J. E. Parks II, V. Schwartz, J. Chen, D.K. Hensley, Enhancing low-temperature activity and durability of Pd-based diesel oxidation catalysts using ZrO_2 supports, Appl. Catal. B Environ. 187 (2016) 181–194, https://doi.org/10.1016/j.apcatb.2016.01.023.
[15] M.J. Hazlett, M. Moses-Debusk, J.E. Parks, L.F. Allard, W.S. Epling, Kinetic and mechanistic study of bimetallic Pt-Pd/Al_2O_3 catalysts for CO and C_3H_6 oxidation, Appl. Catal. B Environ. 202 (2017) 404–417, https://doi.org/10.1016/j.apcatb.2016.09.034.
[16] A. Gremminger, J. Pihl, M. Casapu, J.-D. Grunwaldt, T.J. Toops, O. Deutschmann, PGM based catalysts for exhaust-gas after-treatment under typical diesel, gasoline and gas engine conditions with focus on methane and formaldehyde oxidation, Appl. Catal. B Environ. 265 (2020), 118571, https://doi.org/10.1016/j.apcatb.2019.118571.
[17] J. Kim, Y. Kim, M.H. Wiebenga, S.H. Oh, D.H. Kim, Oxidation of C_3H_8, iso-C_5H_{12} and C_3H_6 under near-stoichiometric and fuel-lean conditions over aged Pt–Pd/Al_2O_3 catalysts with different Pt: Pd ratios, Appl. Catal. B Environ. 251 (2019) 283–294, https://doi.org/10.1016/j.apcatb.2019.04.001.
[18] S.B. Kang, M. Hazlett, V. Balakotaiah, C. Kalamaras, W. Epling, Effect of Pt: Pd ratio on CO and hydrocarbon oxidation, Appl. Catal. B: Environ. 223 (2018) 67–75, https://doi.org/10.1016/j.apcatb.2017.05.057.
[19] D.E.A. Michael, J. Patterson, Noel W. Cant, The effect of carbon monoxide on the oxidation of four C6 to C8 hydrocarbons over platinum, palladium and rhodium, Appl. Catal. B Environ. 26 (2000) 47–57, https://doi.org/10.1016/S0926-3373(00)00110-7.
[20] T.R. Johns, R.S. Goeke, V. Ashbacher, P.C. Thüne, J. Niemantsverdriet, B. Kiefer, C. H. Kim, M.P. Balogh, A.K. Datye, Relating adatom emission to improved durability of Pt–Pd diesel oxidation catalysts, J. Catal. 328 (2015) 151–164, https://doi.org/10.1016/j.jcat.2015.03.016.
[21] C. Carrillo, A. DeLaRiva, H. Xiong, E.J. Peterson, M.N. Spilde, D. Kunwar, R. S. Goeke, M. Wiebenga, S.H. Oh, G. Qi, S.R. Challa, A.K. Datye, Regenerative trapping: How Pd improves the durability of Pt diesel oxidation catalysts, Appl. Catal. B Environ. 218 (2017) 581–590, https://doi.org/10.1016/j.apcatb.2017.06.085.
[22] M. Kaneeda, H. Iizuka, T. Hiratsuka, N. Shinotsuka, M. Arai, Improvement of thermal stability of NO oxidation Pt/Al_2O_3 catalyst by addition of Pd, Appl. Catal. B Environ. 90 (2009) 564–569, https://doi.org/10.1016/j.apcatb.2009.04.011.
[23] J.R.G. Tyne, R. Johns, Eric J. Peterson, Jeffrey T. Miller, Eric A. Stach, Chang H. Kim, Michael P. Balogh, Abhaya K. Datye, Microstructure of bimetallic Pt Pd catalysts under oxidizing conditions, ChemCatChem 5 (2013) 2636–2645, https://doi.org/10.1002/cctc.201300181.
[24] K. Persson, A. Ersson, K. Jansson, J. Fierro, S.G. Järås, Influence of molar ratio on Pd–Pt catalysts for methane combustion, J. Catal. 243 (2006) 14–24, https://doi.org/10.1016/j.jcat.2006.06.019.
[25] H. Xiong, M.H. Wiebenga, C. Carrillo, J.R. Gaudet, H.N. Pham, D. Kunwar, S.H. Oh, G. Qi, C.H. Kim, A.K. Datye, Design considerations for low-temperature hydrocarbon oxidation reactions on Pd based catalysts, Appl. Catal. B Environ. 236 (2018) 436–444, https://doi.org/10.1016/j.apcatb.2018.05.049.
[26] L. Yang, C. Fan, L. Luo, Y. Chen, Z. Wu, Z. Qin, M. Dong, W. Fan, J. Wang, Preparation of Pd/SiO_2 catalysts by a simple dry ball-milling method for lean methane oxidation and probe of the state of active Pd species, Catalysts 11 (2021) 725, https://doi.org/10.3390/catal11060725.
[27] P. Lott, P. Dolcet, M. Casapu, J.-D. Grunwaldt, O. Deutschmann, The effect of prereduction on the performance of Pd/Al_2O_3 and Pd/CeO_2 catalysts during methane oxidation, Ind. Eng. Chem. Res. 58 (2019) 12561–12570, https://doi.org/10.1021/acs.iecr.9b01267.
[28] Johnson Matthey, Price Tables-PMM. http://www.platinum.matthey.com/prices/price-tables (accessed 22 December 2022).
[29] S.L. Greasley, S.J. Page, S. Sirovica, S. Chen, R.A. Martin, A. Riveiro, J.V. Hanna, A. E. Porter, J.R. Jones, Controlling particle size in the Stöber process and incorporation of calcium, J. Colloid Interface Sci. 469 (2016) 213–223, https://doi.org/10.1016/j.jcis.2016.01.065.
[30] C.-H. Liu, K. Giewont, T.J. Toops, E.A. Walker, C. Horvatits, E.A. Kyriakidou, Non-catalytic gas phase NO oxidation in the presence of decane, Fuel 286 (2021), 119388, https://doi.org/10.1016/j.fuel.2020.119388.
[31] I. Mokbel, A. Razzouk, A. Hajjaji, N. Msakni, J. Jose, A gas saturation apparatus for very low vapor or sublimation pressure measurements (10^{-3} Pa): vapor− liquid equilibria of *n*-alkanes (*n*-C_{10}, *n*-C_{24}, *n*-C_{28}), J. Chem. Eng. Data 52 (2007) 1720–1725, https://doi.org/10.1021/je7001122.
[32] X.-Y. Liu, Y. Zhang, M.-X. Gong, Y.-W. Tang, T.-H. Lu, Y. Chen, J.-M. Lee, Facile synthesis of corallite-like Pt–Pd alloy nanostructures and their enhanced catalytic activity and stability for ethanol oxidation, J. Mater. Chem. A 2 (2014) 13840–13844, https://doi.org/10.1039/C4TA02522A.
[33] L.-N. Zhou, X.-T. Zhang, Z.-H. Wang, S. Guo, Y.-J. Li, Cubic superstructures composed of PtPd alloy nanocubes and their enhanced electrocatalysis for methanol oxidation, Chem. Comm. 52 (2016) 12737–12740, https://doi.org/10.1039/C6CC07338G.
[34] Y. Ma, L. Yin, G. Cao, Q. Huang, M. He, W. Wei, H. Zhao, D. Zhang, M. Wang, T. Yang, Pt-Pd bimetal popcorn nanocrystals: enhancing the catalytic performance by combination effect of stable multipetals nanostructure and highly accessible active sites, Small 14 (2018), 1703613, https://doi.org/10.1002/smll.201703613.
[35] T. Cochell, A. Manthiram, Pt@Pd_xCu_y/C core–shell electrocatalysts for oxygen reduction reaction in fuel cells, Langmuir 28 (2012) 1579–1587, https://doi.org/10.1021/la202610z.
[36] T.R. Johns, J.R. Gaudet, E.J. Peterson, J.T. Miller, E.A. Stach, C.H. Kim, M. P. Balogh, A.K. Datye, Microstructure of Bimetallic Pt-Pd Catalysts under Oxidizing Conditions, ChemCatChem 5 (2013) 2636–2645, https://doi.org/10.1002/cctc.201300181.
[37] R. Jervis, N. Mansor, C. Gibbs, C.A. Murray, C.C. Tang, P.R. Shearing, D.J. Brett, Hydrogen oxidation on PdIr/C catalysts in alkaline media, J. Electrochem. Soc. 161 (2014) F458, https://doi.org/10.1149/2.037404jes.
[38] A. Cordero-Borboa, E. Sterling-Black, A. Gómez-Cortés, A. Vazquez-Zavala, X-ray diffraction evidence of the single solid solution character of bi-metallic Pt-Pd catalyst particles on an amorphous SiO_2 substrate, Appl. Surf. Sci. 220 (2003) 169–174, https://doi.org/10.1016/S0169-4332(03)00841-9.
[39] H. He, C. Gao, A general strategy for the preparation of carbon nanotubes and graphene oxide decorated with PdO nanoparticles in water, Molecules 15 (2010) 4679–4694, https://doi.org/10.3390/molecules15074679.
[40] J. Lv, S. Wu, Z. Tian, Y. Ye, J. Liu, C. Liang, Construction of PdO–Pd interfaces assisted by laser irradiation for enhanced electrocatalytic N_2 reduction reaction, J. Mater. Chem. A 7 (2019) 12627–12634, https://doi.org/10.1039/C9TA02045D.
[41] L. Wang, J.-J. Zhai, K. Jiang, J.-Q. Wang, W.-B. Cai, Pd–Cu/C electrocatalysts synthesized by one-pot polyol reduction toward formic acid oxidation: structural characterization and electrocatalytic performance, Int. J. Hydrog. Energy 40 (2015) 1726–1734, https://doi.org/10.1016/j.ijhydene.2014.11.128.
[42] D.B. Bukur, V. Carreto-Vazquez, H.N. Pham, A.K. Datye, Attrition properties of precipitated iron Fischer–Tropsch catalysts, Appl. Catal. A: Gen. 266 (2004) 41–48, https://doi.org/10.1016/j.apcata.2004.01.031.
[43] H. Shinjoh, H. Muraki, Y. Fujitani, Effect of severe thermal aging on noble metal catalysts, Stud. Surf. Sci. Catal. 71 (1991) 617–628, https://doi.org/10.1016/S0167-2991(08)63006-2.
[44] H. Xiong, E. Peterson, G. Qi, A.K. Datye, Trapping mobile Pt species by PdO in diesel oxidation catalysts: Smaller is better, Catal. Today 272 (2016) 80–86, https://doi.org/10.1016/j.cattod.2016.01.022.
[45] J. Schütz, H. Störmer, P. Lott, O. Deutschmann, Effects of hydrothermal aging on CO and NO oxidation activity over monometallic and bimetallic Pt-Pd catalysts, Catalysts 11 (2021) 300, https://doi.org/10.3390/catal11030300.
[46] Y. Ryou, J. Lee, S.J. Cho, H. Lee, C.H. Kim, D.H. Kim, Activation of Pd/SSZ-13 catalyst by hydrothermal aging treatment in passive NO adsorption performance at low temperature for cold start application, Appl. Catal. B Environ. 212 (2017) 140–149, https://doi.org/10.1016/j.apcatb.2017.04.077.
[47] F. Lewis, The hydrides of palladium and palladium alloys, Platinum Met. Rev. 5 (1961) 21–25. https://citeseerx.ist.psu.edu/viewdoc/download?doi=10.1.1.548.1909&rep=rep1&type=pdf.
[48] Y. Kim, J. Kim, D.H. Kim, Investigation on the enhanced catalytic activity of a Ni-promoted Pd/C catalyst for formic acid dehydrogenation: effects of preparation methods and Ni/Pd ratios, RSC Adv. 8 (2018) 2441–2448, https://doi.org/10.1039/C7RA13150J.
[49] C.-P. Hwang, C.-T. Yeh, Platinum-oxide species formed by oxidation of platinum crystallites supported on alumina, J. Mol. Catal. A Chem. 112 (1996) 295–302, https://doi.org/10.1016/1381-1169(96)00127-6.
[50] C. Carrillo, T.R. Johns, H. Xiong, A. DeLaRiva, S.R. Challa, R.S. Goeke, K. Artyushkova, W. Li, C.H. Kim, A.K. Datye, Trapping of mobile Pt species by PdO nanoparticles under oxidizing conditions, J. Phys. Chem. Lett. 5 (2014) 2089–2093, https://doi.org/10.1021/jz5009483.
[51] J.E. Etheridge, T.C. Watling, A.J. Izzard, M.A. Paterson, The effect of Pt: Pd ratio on light-duty diesel oxidation catalyst performance: an experimental and modelling study, SAE Int. J. Engines 8 (2015) 1283–1299, https://doi.org/10.4271/2015-01-1053.